Simultaneous wind and rainfall detection by power spectrum analysis using a VAD scanning coherent Doppler lidar

TIANWEN WEI,[1] HAIYUN XIA,[1,2,5] JIANJUN HU,[3,6] CHONG WANG,[1] MINGJIA SHANGGUAN,[1] LU WANG,[1] MINGJIAO JIA,[1] (iD) AND XIANKANG DOU[1,2,4]

[1]*School of Earth and Space Science, USTC, Hefei 230026, China*
[2]*CAS Center for Excellence in Comparative Planetology, Hefei 230026, China*
[3]*School of Optoelectronic Science and Engineering, Soochow University, Suzhou 215006, China*
[4]*School of Electronic Information, Wuhan University, Wuhan 430072, China*
[5]*hsia@ustc.edu.cn*
[6]*jianjunhu@suda.edu.cn*

Abstract: Doppler wind lidar is an effective tool for wind detection with high temporal and spatial resolution. However, precise wind profile measurement under rainy conditions is a challenge, due to the interfering signals from raindrop reflections. In this work, a compact all-fiber coherent Doppler lidar (CDL) at working wavelength of 1.5 μm is applied for simultaneous wind and precipitation detection. The performance of the lidar is validated by comparison with the weather balloons. Thanks to the ability of precise spectrum measurement, both aerosol and rainfall signals can be detected by the CDL under rainy conditions. The spectrum width is used to identify the precipitation events, during which the two-peak Doppler spectrum is observed. The spectrum is fitted by a two-component Gaussian model and two velocities are obtained. By using the velocity-azimuth display (VAD) scanning technique, wind speed and rainfall speed are simultaneously retrieved. The false detection probability of wind speed in the rainy conditions is thus reduced.

1. Introduction

Researches on precipitation have attracted interests as it plays an important role in many fields [1,2], such as flight safety [3], extreme weather warning [4], agricultural meteorology [5] and hydrological cycle [6]. On the other hand, wind profile detection, especially under rainy condition, is also meaningful in above fields. For example, in aviation flights, the microburst and wind shear that often occur during thunderstorm conditions may significantly break the airplane's balance [7]. The freezing precipitation may cause aircraft icing, which will greatly decrease the lift-to-drag ratio and deteriorate the aircraft's aerodynamic performance, even resulting in an aviation accident when serious [8,9]. Accurate measurement of wind and rainfall will be helpful for improving flight safety [10,11].

Several instruments have been used for wind and(or) rainfall detection, such as Vaisala weather station [12], microwave radar [13–15] and lidar [16–18]. Vaisala is limited to the ground level measurements. Radars suffer from the disadvantages of wide beamwidth [19]. Doppler wind lidar (DWL) is an effective tool for wind detection with high temporal and spatial resolution [20–22]. However, precise wind field measurement under rainy conditions is a challenge, due to the presence of interfering signals from raindrop reflections [23]. When the rain is too heavy, the backscattering signal is weakened due to strong attenuation of raindrops and decreasing of aerosols. Furthermore, the raindrops on the receiver lens cause serious wavefront distortion, leading to low heterodyne detection efficiency of the coherent Doppler lidar (CDL).

There are two fundamental detection methods in DWL, direct detection and coherent detection. In direct detection Doppler lidar (DDL), an optical frequency discriminator or spectrum analyzer is often used to convert Doppler shift into power fluctuation or optical pattern change [24–27]. In CDL, a local oscillator is used to mix with the backscattering signal, and precise Doppler-shift spectrum can be obtained [28–32].

Under clear days, both the CDL and the DDL can be used to detect wind field with high precision [33]. However, under rainy condition, a two-peak Doppler spectrum originating from backscattering of aerosols and raindrops are observed [34,35]. In the DDL, a known signal spectrum profile is assumed when retrieving the wind speed. Therefore, it is difficult to find an unknown rainfall signal. In previous work, a fiber Fabry-Perot scanning interferometer (FFP-SI) is used to obtain the signal spectrum in the high spectral resolution wind lidar (HSRWL) [36]. The sampling of each entire spectrum takes 1 minute when considering 30 steps, resulting in low temporal resolution. The ability of precise spectrum measurement with high temporal and spatial resolution makes the CDL suitable for wind and rainfall detection. Some researchers have tried to use the CDL to retrieve the raindrop size distribution from vertical measurements [37,38].

In this work, a compact all-fiber CDL is applied for simultaneous detection of the wind field and rainfall in precipitation events. The accuracy of the lidar is validated by comparison with the radiosonde, under clear-air conditions. Two-peak Doppler spectrum is observed during precipitation events. By using the VAD scanning technique, radial wind velocity and rainfall velocity are well separated.

2. Principle

Under rainy conditions, the received backscattering signal may contain two components, the aerosol signal and rainfall signal. From the Doppler power spectrum, two peaks can be observed if the wind and the rainfall velocities are different. A two-component Gaussian model is often used to fit the two-peak spectrum [34]:

$$S(f) = I_a \exp\left[-\frac{(f-f_a)^2}{2\sigma_a^2}\right] + I_r \exp\left[-\frac{(f-f_r)^2}{2\sigma_r^2}\right], \tag{1}$$

where f_a and f_r are the mean Doppler frequency shift from aerosols and raindrops, respectively, I_a and I_r are the peak intensity, σ_a and σ_r are the spectrum width. A least squares fit is applied to determine the above parameters. Generally, the intensity of the rainfall signal has a positive relation to the precipitation rate. Thus, under different rain conditions, there may be different relative intensities between the rainfall signal and the aerosol signal. For example, in the light rain events, small raindrops will be easily driven by the wind and the precipitation spectrum is difficult to be distinguished due to its weak intensity and close location to the aerosol spectrum. When the rain becomes large, the two signals may have similar intensity and can be well identified.

The signal spectrum width is mainly determined by the intrinsic linewidth of the transmitted pulse [39]. It is broadened by some factors, such as Brownian motion, wind turbulence and so on. For aerosol particles, the Brownian velocity standard deviation is on the order of 1 mm/s, which can be neglected compared to the spectrum width caused by turbulence [40]. For raindrops, the Doppler spectrum width is additionally broadened due to the different terminal velocity of different raindrop size. The individual signals from different size raindrops have the same spectrum width but different Doppler shift. Therefore, the overlap of these signals will result in a broadened Doppler-shift spectrum. It is used as one of the bases in separating wind and rainfall signal.

The windowing effect due to the finite length of data also broaden the spectrum. In the CDL, the Doppler power spectrum is estimated from the periodogram [41]

$$\hat{P}(m) = \frac{T_s}{M}\left|\sum_{k=0}^{M-1} z_k \exp(-\frac{2\pi ikm}{M})\right|^2, \qquad (2)$$

where z is the sampling sequence with length M, and T_s is the sampling interval. The value of M is chosen according to the pulse duration, which determines the minimum spatial resolution. In practice, incoherent accumulation between a large number of pulses at the same range gate is usually applied to improve the detection probability and velocity estimation accuracy [42,43]. The line of sight (LOS) velocity is given by the following relationship:

$$V_{\mathrm{LOS}} = \frac{\lambda}{2}f_i, \qquad (3)$$

where $f_{i=a,r}$ is the mean Doppler frequency shift for aerosols and raindrops. The sign is defined as positive when the movement is toward the lidar, and vice versa.

3. Instrument

The 1.5 µm laser shows the highest maximum permissible exposure in the wavelength ranging from 0.3 to 10 µm [44,45]. A compact micro-pulse CDL at operating wavelength of 1.5 µm is applied in this work. The pulse energy and pulse duration of the laser are 100 µJ and 300 ns, respectively. A double D-shaped telescope is employed for the purpose of easy alignment and compressing blind zone. It is made up of two aspheric lenses that are glued together along parallel optical axes [46]. The absolute overlap distance and blind distance are 1 km and 30 m, respectively. Controlling software is developed to achieve real-time signal processing and unattended operation. The adoption of all-fiber architecture and temperature control subsystem makes it possible for the lidar to work well in different weather conditions. The system parameters are summarized in Table 1.

Table 1. Key parameters of the lidar system

	Parameter	Value
Laser	Wavelength (nm)	1548
	Pulse energy (µJ)	100
	Pulse duration (ns)	300
	Repetition frequency (kHz)	10
Telescope	Diameter (mm)	80
Scanner	Radial temporal resolution (s)	2
	Azimuth scanning range (°)	0-360
	Zenith scanning range (°)	0-90

4. Experiments

Two experiments are presented in this section. First, the comparison experiment between the lidar and radiosonde. Second, the observation experiment during a precipitation event using the lidar combined with the VAD scanning technique. Two-peak Doppler spectrum is observed and both wind and rainfall velocity are simultaneously obtained.

4.1. Comparison with the radiosonde

To validate the performance of the lidar system, a comparison experiment is carried out from August 16th to September 5th, 2018, at National Meteorological Observing Station of Anqing (30.53 °N, 117.05 °E), one of the 120 operational radiosonde stations in mainland China. GTS1 digital radiosonde carried by weather balloons is launched twice a day at 07:15 and 19:15. The wind speed and direction were measured by tracing the GTS1 using L-band secondary wind-finding radar [47,48].

During the experiment, the lidar works in a Doppler beam-swinging (DBS) scanning mode which has three pointing directions. The one is vertical direction, while the other two are north and west with an elevation angle of 60°. Then the horizontal wind speed and direction are calculated from three radial wind profiles based on the assumption of horizontally homogeneous wind field. The duration for each horizontal wind measurement is 42 s and the vertical spatial resolution is 52 m. The ability of continuous observation is confirmed, and typical results during sunny condition are given in Fig. 1. Strengthening horizontal wind speed and wind shear can be seen clearly at an altitude of about 0.5 km. Long-term continuous observation is reported elsewhere [49].
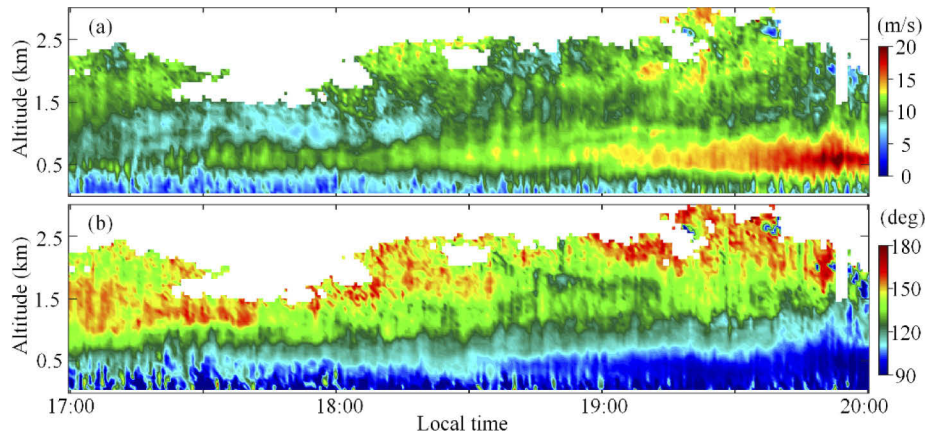

Fig. 1. Continuous observation results on August 16th, 2018. (a) Time-height plot of horizontal wind speed and (b) horizontal wind direction.

Figure 2 shows two typical comparison results with the radiosonde. The arising time of the balloons depends on local conditions. Typically, it will take 5–10 minutes to access an altitude of 3 km. In order to suppress the statistical standard error, the time resolution of the lidar data is averaged for 5 minutes and three horizontal wind profiles in time sequence are plotted for comparison. The wind speed and direction derived from the CDL and radiosonde show good consistency in Fig. 2. However, there are some differences between the two results at low altitude. The inhomogeneity of the wind field may be the main reason.

Statistical analysis of wind differences between the lidar and radiosonde is shown in Fig. 3. For each balloon's speed or direction, three corresponding lidar data at the same altitude after the balloon's release time are chosen. Totally 429 available samples are obtained during the experiment. The mean differences of wind speed and direction are 0.3 m/s and 1.1°, respectively. The standard deviations of wind speed and direction are 0.84 m/s and 9.2°, respectively. The results validate the performance of the lidar.
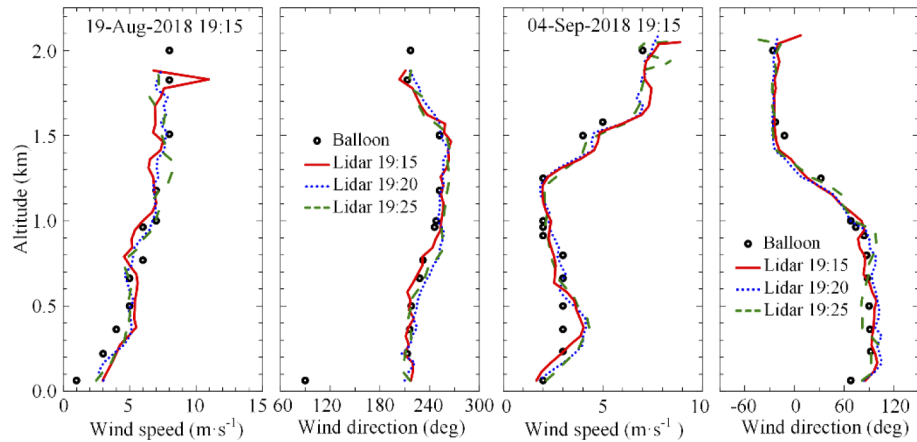
Fig. 2. Horizontal wind and direction profiles measured by Doppler wind lidar and radiosonde.
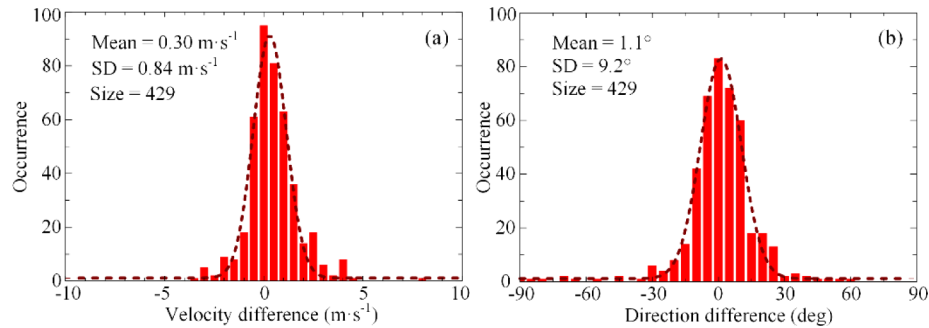

Fig. 3. Statistics of the difference in wind measurements between the lidar and radiosonde (dash lines are the Gaussian fit results to the data). (a) Histogram distributions of velocity difference and (b) direction difference.

4.2. Experiment during precipitation event

The experiment is carried out on 13 May 2019 at the campus of the University of Science and Technology of China (31.83°N, 117.25°E). The precipitation begins at 16:30 and stops at about 17:00. The VAD scanning technique is applied. The azimuth scanning range is set as 0–270° to avoid the nearby building and the elevation angle is 60°. The angle interval is 5° and a total of 54 radial profiles are obtained for each scanning process, lasting 135 s. The radial measurement results are shown in Fig. 4.

The wideband carrier-to-noise ratio (CNR) as shown in Fig. 4(a) is the ratio of total signal power to noise power over the entire spectral bandwidth. The accuracy of velocity estimation is mainly determined by the value of CNR [50]. Figure 4(b) shows the spectrum width estimated by the ratio of power integration over the frequency span to the peak power value. The spectrum will be broadened if more than one peaks exist.

The aerosol concentration represented by the CNR is relatively large before the rainfall, and decreases along with the rising clouds. The rainfall scavenges most of the aerosol particles, resulting in a sharp reduction of both the aerosol concentration and the maximum detection range when the precipitation begins. The Doppler spectrum width shows large value during the precipitation, as shown in Fig. 4(b), which means that the aerosol signal and rainfall signal are detected simultaneously.
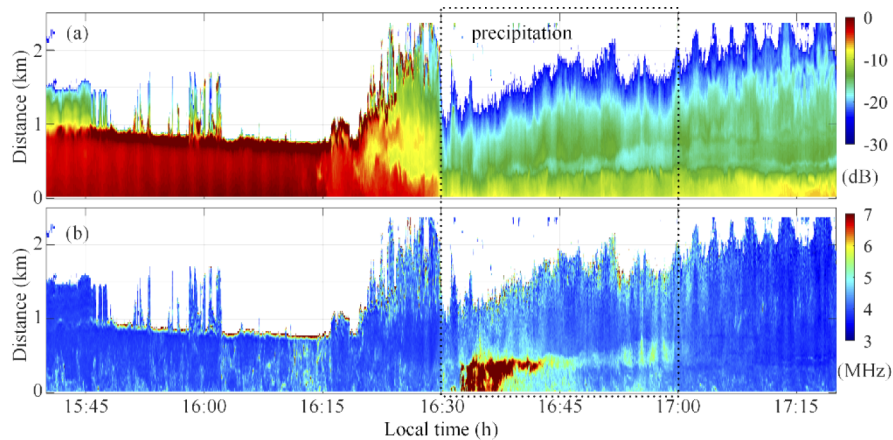
Fig. 4. Results of the lidar during a precipitation event on 13 May 2019. (a) Wideband carrier-to-noise ratio; (b) Signal spectrum width.

For further analysis, two typical power spectra in sunny and rainy conditions are given in Figs. 5(a) and 5(b). The spectrum in rainy condition shows an obvious difference. Three spectra examples of Fig. 5(b) at different distances are given in Figs. 5(c)–(e). Two-peak structure spectra are observed. The two-component Gaussian model as described in Sect. 2 is applied to fit these spectra.
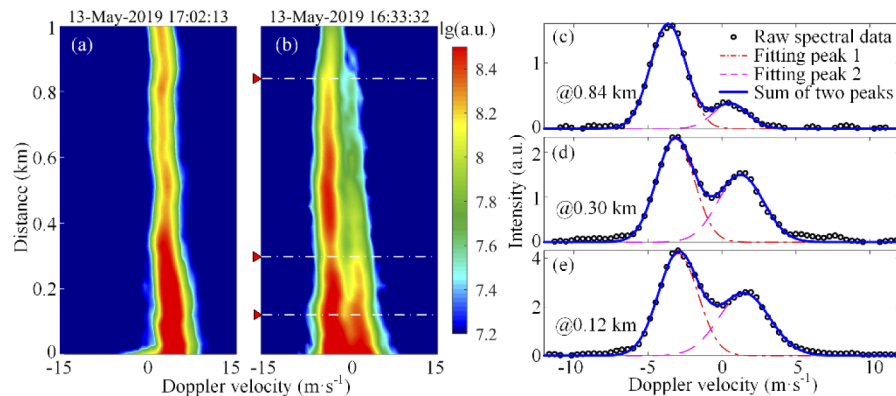

Fig. 5. Comparison of the signal power spectrum between sunny (a) and rainy (b) conditions. Specific spectra and two-component Gaussian fitting curves at the distance of (c) 0.84 km; (d) 0.30 km; (e) 0.12 km. The position of the spectra (c)–(e) are marked in (b) with white dotted lines.

The wind detection accuracy is determined by the CNR of the CDL. However, in the wind retrieval process during rainy conditions, there is a difference between wind results inferred from the one-peak and two-peak analyses. For example, in Fig. 5(d), the intensity of rainfall spectrum is similar to that of aerosol spectrum. Wind speed estimation using one-peak analysis will lead to false detection results.

In order to identify which peak is the aerosol signal and which one is the rainfall signal, some separation methods should be given. Thanks to the VAD scanning technique as shown in Fig. 6(a), the problem can be solved. Assuming the velocity vector and unit vector of the lidar direction are

given by

$$\begin{cases} \vec{V} = (V_\parallel \cos\theta_0, V_\parallel \sin\theta_0, V_\perp) \\ \vec{n} = (\cos\varphi_0 \cos\theta, \cos\varphi_0 \sin\theta, \sin\varphi_0) \end{cases}, \tag{4}$$

respectively, where $V_\parallel$ and $V_\perp$ are the horizontal and vertical wind speed, respectively, θ_0 is the horizontal wind direction, θ is the azimuth angle of the lidar, φ_0 is the elevation angle of the lidar and in this case is a constant value of $60°$. The LOS velocity detected by the lidar is then given by

$$V_{\text{LOS}} = -\vec{V} \cdot \vec{n} = -(V_\parallel \cos\theta_0 \cos\varphi_0 \cos\theta + V_\parallel \sin\theta_0 \cos\varphi_0 \sin\theta + V_\perp \sin\varphi_0).$$
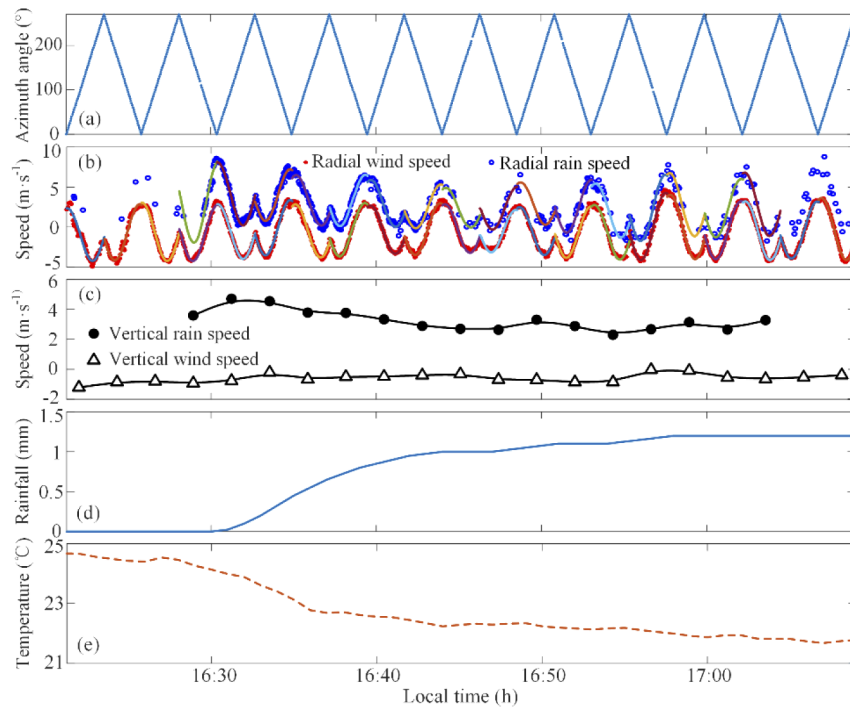$$= -\cos\varphi_0 [V_\parallel \cos(\theta - \theta_0) + V_\perp \tan\varphi_0] \tag{5}$$

Fig. 6. (a) Lidar's azimuth angle; (b) The separated radial wind speed and rain speed and their sine wave fitting results at the distance of 510 m; (c) Vertical wind speed and rain speed; (d) Accumulated rainfall; (e) Temperature.

Equation (5) shows that the LOS velocity is a cosine function of the lidar's azimuth angle, based on the assumption that the wind and rainfall velocity vectors are homogeneous at the same altitude and keep constant during each scanning loop.

If the horizontal wind and horizontal rain speed have the similar value and direction. It will be easy to separate the two spectra, since a large vertical speed of rain will move positive its cosine pattern of LOS velocity during the scanning. But when the rain is light, the vertical speed is small. It would be difficult to tell which spectrum is associated with the rain. Furthermore, the wind changes along the altitude, including its value and direction. And, the horizontal speed of rain will follow the change of wind. For example, if the raindrops are dragged by the wind and still in accelerating process, the difference in horizontal speeds may result in ambiguous LOS speeds.

To deal with this problem, the following steps are used to analyze the two-peak spectra in each line of sight.

1. In rainy condition, two-peak Gaussian fitting is applied to the raw spectrum data. If the fitting leads to bad results, turn to normal one-peak fitting.

2. In general, the horizontal rain speed is similar to the wind speed. A large vertical rain speed will cause an obvious additional LOS Doppler shift. Thus the right spectrum is tagged as the rain signal.

3. In case of light rain, the peaks are close to each other. Compare the width of the fitting values. The wider peak is considered as rainfall signal. The size distribution of the raindrops will broaden the spectrum of rain. While, the broadening effect associated with the aerosol is negligible.

4. For each scanning loop, fit the wind speed and rain speed using a cosine function, respectively.

Figure 6 gives an example of cosine wave fitting results of the LOS speeds. For each scanning loop, if the number of available rain speed is less than 20% of the total number, the fitting results are regarded as unreliable. As shown in Fig. 6(b), the radial wind speed fluctuates around zero during the scanning, which means that the vertical wind speed is small. The vertical wind speed and rain speed are plotted in Fig. 6(c). The rainfall and temperature detected by using a Davis weather station (wireless vantage pro2 plus) is plotted in Fig. 6(d) and Fig. 6(e), with a temporal resolution of 1 minute. The real-time rain rate (the derivative of the accumulated rainfall) shows a similar trend with the vertical rain speed, that is the vertical rain speed decreases as the rain
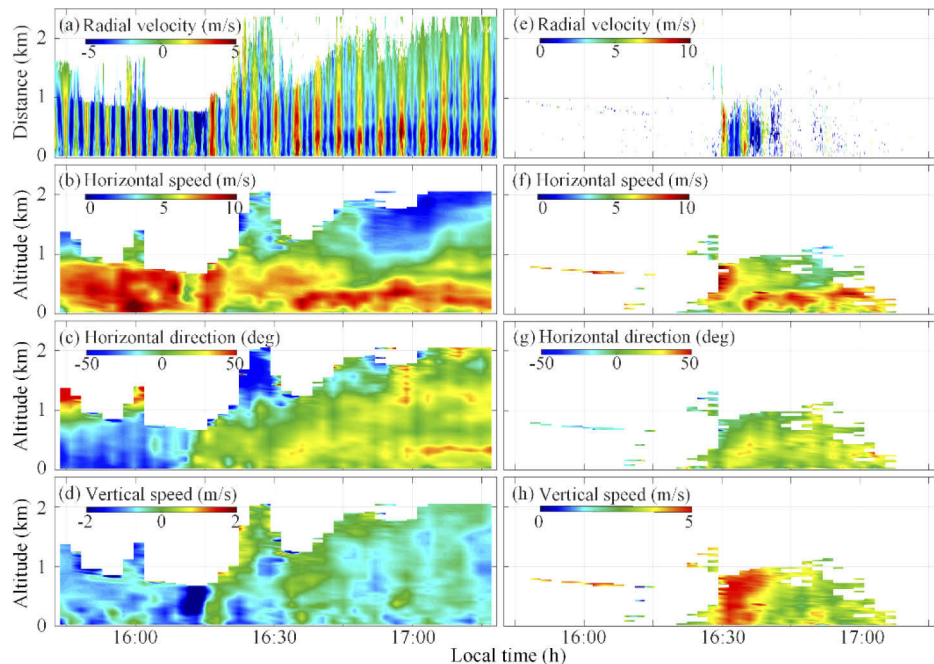

Fig. 7. (a) The separated radial wind speed; (b) Horizontal wind speed; (c) Horizontal wind direction; (d) Vertical wind speed. (e) The separated radial rain speed; (f) Horizontal rain speed; (g) Horizontal rain direction; (h) Vertical rain speed.

rate decreases. This is consistent with our common sense that heavy rain is often accompanied by big raindrops which have large falling speed, but light rain usually consists of small drops.

As an example, the rain speed and wind speed in rainy condition are given in Fig. 7. To estimate the influence of rain to the wind retrieval results, in this case, the difference of the radial wind velocity retrieved from one-peak or two-peak methods are compared. A LOS speed difference over 2 m/s is obtained. In other words, the two-peak fitting method can reduce the false wind detection probability in rainy conditions. As expected, the wind and rain show similar horizontal trends both in speed and direction, as shown in Fig. 7.

As shown in Fig. 7(d), there is an enhanced upward wind speed at 16:15. At the same time, the horizontal wind direction changes from −20° to 30° (0° corresponds to the north wind and the degree increases in clockwise), as shown in Fig. 7(c). Considering the decreasing temperature and rising clouds, it is reasonable to regard this precipitation process as frontal rainfall caused by the interaction between the cold front and warm front. The vertical rain speed reaches about 5 m/s at the beginning of precipitation and decreases to 2 m/s as the rain rate decrease.

5. Conclusion

Wind and rain speed were simultaneously retrieved using a compact all-fiber CDL operating in the VAD scanning mode during a precipitation event. The comparison experiments with weather balloons validated the lidar's accuracy and stability.

In rainy conditions, the two-peak Gaussian model was fit to the spectrum for separating the aerosol signal and rain signal. Usually, the rain spectrum is shifted to the right edge of the aerosol spectrum in the frequency domain, due to the vertical speed of raindrops. In case of drizzling rain, the wider spectrum is labeled as the rain signal.

The separation of rain speed and wind speed will provide information for microphysical rain studies. For future work, we will compare the detection results from CDL and radar [13–15]. We also plan to combine Mie lidars at different working wavelengths [51,52], depolarization lidars [53–55], Raman lidar for water vapor and temperature detection [56–60] and Doppler lidar for further investigation of different precipitations, such as rainfall, sleet, hail, snow.

References

1. A. Y. Hou, R. K. Kakar, S. Neeck, A. A. Azarbarzin, C. D. Kummerow, M. Kojima, R. Oki, K. Nakamura, and T. Iguchi, "The global precipitation measurement mission," Bull. Am. Meteorol. Soc. **95**(5), 701–722 (2014).
2. C. Kidd and G. Huffman, "Global precipitation measurement," Met. Apps **18**(3), 334–353 (2011).
3. J. Luers and P. Haines, "Heavy rain influence on airplane accidents," J. Aircr. **20**(2), 187–191 (1983).
4. L. Alfieri and J. Thielen, "A European precipitation index for extreme rain-storm and flash flood early warning," Met. Apps **22**(1), 3–13 (2015).
5. Y. Bayissa, T. Tadesse, G. Demisse, and A. Shiferaw, "Evaluation of Satellite-Based Rainfall Estimates and Application to Monitor Meteorological Drought for the Upper Blue Nile Basin, Ethiopia," Remote Sens. **9**(7), 669 (2017).
6. U. Schneider, P. Finger, A. Meyer-Christoffer, E. Rustemeier, M. Ziese, and A. Becker, "Evaluating the Hydrological Cycle over Land Using the Newly-Corrected Precipitation Climatology from the Global Precipitation Climatology Centre (GPCC)," Atmosphere **8**(12), 52 (2017).
7. P. Chan and Y. Lee, "Application of short-range lidar in wind shear alerting," J. Atmos. Oceanic Technol. **29**(2), 207–220 (2012).
8. Y. Cao, Z. Wu, and Z. Xu, "Effects of rainfall on aircraft aerodynamics," Prog. Aerosp. Sci. **71**, 85–127 (2014).
9. B. C. Bernstein, T. A. Omeron, M. K. Politovich, and F. McDonough, "Surface weather features associated with freezing precipitation and severe in-flight aircraft icing," Atmos. Res. **46**(1-2), 57–73 (1998).
10. C. J. O'Connor and D. K. Rutishauser, "Enhanced Airport Capacity Through Safe, Dynamic Reductions in Aircraft Separation: NASA's Aircraft Vortex Spacing System (AVOSS)," (2001).
11. A. Dolfi-Bouteyre, B. Augere, M. Valla, D. Goular, D. Fleury, G. Canat, C. Planchat, T. Gaudo, C. Besson, and A. Gilliot, "Aircraft wake vortex study and characterization with 1.5 μm fiber Doppler lidar," (2009).
12. J. Reuder, M. Ablinger, H. Agústsson, P. Brisset, S. Brynjólfsson, M. Garhammer, T. Jóhannesson, M. O. Jonassen, R. Kühnel, and S. Lämmlein, "FLOHOF 2007: An overview of the mesoscale meteorological field campaign at Hofsjökull, Central Iceland," Meteorol. Atmos. Phys. **116**(1-2), 1–13 (2012).

13. G. Peters, B. Fischer, and T. Andersson, "Rain observations with a vertically looking Micro Rain Radar (MRR)," Boreal Environ. Res. **7**, 353–362 (2002).
14. T. N. Rao, D. N. Rao, and S. Raghavan, "Tropical precipitating systems observed with Indian MST radar," Radio Sci. **34**(5), 1125–1139 (1999).
15. H. Qing, Y. Chu, Z. Zhao, C. Su, C. Zhou, and Y. Zhang, "Observation and analysis of atmospheric rainfall based on the very high frequency radar," IET Radar, Sonar & Navigation **11**(4), 616–620 (2017).
16. P. A. Lewandowski, W. E. Eichinger, A. Kruger, and W. F. Krajewski, "Lidar-Based Estimation of Small-Scale Rainfall: Empirical Evidence," J. Atmos. Oceanic Technol. **26**(3), 656–664 (2009).
17. C. Wang, M. Jia, H. Xia, Y. Wu, T. Wei, X. Shang, X. Xue, X. Dou, C. Yang, X. Xue, and X. Dou, "Relationship Analysis of PM2.5 and BLH using Aerosol and Turbulence Detection Lidar," Atmos. Meas. Tech. **12**(6), 3303–3315 (2019).
18. S. Lolli, E. J. Welton, and J. R. Campbell, "Evaluating Light Rain Drop Size Estimates from Multiwavelength Micropulse Lidar Network Profiling," J. Atmos. Oceanic Technol. **30**(12), 2798–2807 (2013).
19. E. J. O'Connor, R. J. Hogan, and A. J. Illingworth, "Retrieving Stratocumulus Drizzle Parameters Using Doppler Radar and Lidar," J. Appl. Meteorol. **44**(1), 14–27 (2005).
20. C. J. Grund, R. M. Banta, J. L. George, J. N. Howell, M. J. Post, R. A. Richer, and A. M. Weickmann, "High-resolution doppler lidar for boundary layer and cloud research," J. Atmos. Oceanic Technol. **18**(3), 376–393 (2001).
21. G. J. Koch, J. Y. Beyon, P. E. Petzar, M. Petros, J. Yu, B. C. Trieu, M. J. Kavaya, U. N. Singh, E. A. Modlin, and B. W. Barnes, "Field testing of a high-energy 2-μm Doppler lidar," J. Appl. Remote Sens **4**(1), 043512 (2010).
22. H. Xia, M. Shangguan, C. Wang, G. Shentu, J. Qiu, Q. Zhang, X. Dou, and J. Pan, "Micro-pulse upconversion Doppler lidar for wind and visibility detection in the atmospheric boundary layer," Opt. Lett. **41**(22), 5218 (2016).
23. M. L. Aitken, M. E. Rhodes, and J. K. Lundquist, "Performance of a wind-profiling lidar in the region of wind turbine rotor disks," J. Atmos. Oceanic Technol. **29**(3), 347–355 (2012).
24. H. Xia, X. Dou, D. Sun, Z. Shu, X. Xue, Y. Han, D. Hu, Y. Han, and T. Cheng, "Mid-altitude wind measurements with mobile Rayleigh Doppler lidar incorporating system-level optical frequency control method," Opt. Express **20**(14), 15286 (2012).
25. M. Shangguan, H. Xia, X. Dou, C. Wang, J. Qiu, Y. Zhang, Z. Shu, and X. Xue, "Comprehensive wind correction for a Rayleigh Doppler lidar from atmospheric temperature and pressure influences and Mie contamination," Chin. Phys. B **24**(9), 094212 (2015).
26. H. Xia, X. Dou, M. Shangguan, R. Zhao, D. Sun, C. Wang, J. Qiu, Z. Shu, X. Xue, Y. Han, and Y. Han, "Stratospheric temperature measurement with scanning Fabry-Perot interferometer for wind retrieval from mobile Rayleigh Doppler lidar," Opt. Express **22**(18), 21775 (2014).
27. O. Lux, C. Lemmerz, F. Weiler, U. Marksteiner, B. Witschas, S. Rahm, A. Schäfler, and O. Reitebuch, "Airborne wind lidar observations over the North Atlantic in 2016 for the pre-launch validation of the satellite mission Aeolus," Atmos. Meas. Tech. **11**(6), 3297–3322 (2018).
28. R. T. Menzies and R. M. Hardesty, "Coherent Doppler lidar for measurements of wind fields," Proc. IEEE **77**(3), 449–462 (1989).
29. S. Kameyama, T. Ando, K. Asaka, Y. Hirano, and S. Wadaka, "Compact all-fiber pulsed coherent Doppler lidar system for wind sensing," Appl. Opt. **46**(11), 1953 (2007).
30. G. J. Koch, J. Y. Beyon, B. W. Barnes, M. Petros, J. Yu, F. Amzajerdian, M. J. Kavaya, and U. N. Singh, "High-energy 2 μm Doppler lidar for wind measurements," Opt. Eng. **46**(11), 116201 (2007).
31. W. Diao, X. Zhang, J. Liu, X. Zhu, Y. Liu, D. Bi, and W. Chen, "All fiber pulsed coherent lidar development for wind profiles measurements in boundary layers," Chin. Opt. Lett. **12**(7), 072801 (2014).
32. P. Achtert, I. M. Brooks, B. J. Brooks, B. I. Moat, J. Prytherch, P. O. G. Persson, and M. Tjernström, "Measurement of wind profiles by motion-stabilised ship-borne Doppler lidar," Atmos. Meas. Tech. **8**(9), 9339–9372 (2015).
33. M. Shangguan, H. Xia, C. Wang, J. Qiu, S. Lin, X. Dou, Q. Zhang, and J.-W. Pan, "Dual-frequency Doppler lidar for wind detection with a superconducting nanowire single-photon detector," Opt. Lett. **42**(18), 3541 (2017).
34. B. T. Lottman, R. G. Frehlich, S. M. Hannon, and S. W. Henderson, "Evaluation of Vertical Winds near and inside a Cloud Deck Using Coherent Doppler Lidar," J. Atmos. Oceanic Technol. **18**(8), 1377–1386 (2001).
35. N. Kalthoff, B. Adler, A. Wieser, M. Kohler, K. Träumner, J. Handwerker, U. Corsmeier, S. Khodayar, D. Lambert, A. Kopmann, N. Kunka, G. Dick, M. Ramatschi, J. Wickert, and C. Kottmeier, "KITcube-a mobile observation platform for convection studies deployed during HyMeX," Meteorol. Z. **22**(6), 633–647 (2013).
36. M. Shangguan, H. Xia, C. Wang, J. Qiu, G. Shentu, Q. Zhang, X. Dou, and J. W. Pan, "All-fiber upconversion high spectral resolution wind lidar using a Fabry-Perot interferometer," Opt. Express **24**(17), 19322 (2016).
37. M. Aoki, H. Iwai, K. Nakagawa, S. Ishii, and K. Mizutani, "Measurements of Rainfall Velocity and Raindrop Size Distribution Using Coherent Doppler Lidar," J. Atmos. Oceanic Technol. **33**(9), 1949–1966 (2016).
38. K. Träumner, J. Handwerker, A. Wieser, and J. Grenzhäuser, "A Synergy Approach to Estimate Properties of Raindrop Size Distributions Using a Doppler Lidar and Cloud Radar," J. Atmos. Oceanic Technol. **27**(6), 1095–1100 (2010).
39. R. Frehlich, "Performance of maximum likelihood estimators of mean power and doppler velocity with a priori knowledge of spectrum width," J. Atmos. Oceanic Technol. **16**(11), 1702–1709 (1999).
40. T. Fujii and T. Fukuchi, Laser Remote Sensing (CRC Press, 2005).
41. R. G. Frehlich and M. J. Yadlowsky, "Performance of Mean-Frequency Estimators for Doppler Radar and Lidar," J. Atmos. Oceanic Technol. **11**(5), 1217–1230 (1994).

42. B. J. Rye and R. M. Hardesty, "Discrete spectral peak estimation in incoherent backscatter heterodyne lidar. I. Spectral accumulation and the Cramer-Rao lower bound," IEEE Trans. Geosci. Electron. **31**(1), 16–27 (1993).

43. B. J. Rye and R. M. Hardesty, "Discrete spectral peak estimation in incoherent backscatter heterodyne lidar. II. Correlogram accumulation," IEEE Trans. Geosci. Electron. **31**(1), 28–35 (1993).

44. H. Xia, G. Shentu, M. Shangguan, X. Xia, X. Jia, C. Wang, J. Zhang, J. S. Pelc, M. M. Fejer, Q. Zhang, X. Dou, and J. W. Pan, "Long-range micro-pulse aerosol lidar at 1.5 μm with an upconversion single-photon detector," Opt. Lett. **40**(7), 1579 (2015).

45. ANSI Standard Z136.1, American National Standard for the Safe Use of Lasers (American National Standards Institute, Inc., 2007).

46. C. Wang, H. Xia, Y. Wu, J. Dong, T. Wei, L. Wang, and X. Dou, "Meter-scale spatial-resolution-coherent Doppler wind lidar based on Golay coding," Opt. Lett. **44**(2), 311 (2019).

47. J. Bian, "Statistics of gravity waves in the lower stratosphere over Beijing based on high vertical resolution radiosonde," Sci. China, Ser. D: Earth Sci. **48**(9), 1548 (2005).

48. S. D. Zhang and F. Yi, "A statistical study of gravity waves from radiosonde observations at Wuhan (30° N, 114° E) China," Ann. Geophys. **23**(3), 665–673 (2005).

49. M. Jia, J. Yuan, C. Wang, H. Xia, Y. Wu, L. Zhao, T. Wei, J. Wu, L. Wang, S. Y. Gu, L. Liu, D. Lu, R. Chen, X. Xue, and X. Dou, "Long-live High Frequency Gravity Wavesin Atmospheric Boundary Layer: Observations and Simulations," *Atmos. Chem. Phys. Discuss.*, 1–27 (2019).

50. R. Frehlich, "Simulation of Coherent Doppler Lidar Performance in the Weak_Signal Regime," J. Atmos. Oceanic Technol. **13**(3), 646–658 (1996).

51. X. Shang, H. Xia, X. Dou, M. Shangguan, M. Li, and C. Wang, "Adaptive inversion algorithm for 1.5 μm visibility lidar incorporating in situ Angstrom wavelength exponent," Opt. Commun. **418**, 129–134 (2018).

52. H. Xia, D. Sun, Y. Yang, F. Shen, J. Dong, and T. Kobayashi, "Fabry-Perot interferometer based Mie Doppler lidar for low tropospheric wind observation," Appl. Opt. **46**(29), 7120 (2007).

53. J. Qiu, H. Xia, M. Shangguan, X. Dou, M. Li, C. Wang, X. Shang, S. Lin, and J. Liu, "Micro-pulse polarization lidar at 1.5 μm using a single superconducting nanowire single-photon detector," Opt. Lett. **42**(21), 4454 (2017).

54. L. R. Bissonnette, G. Roy, and F. Fabry, "Range–Height Scans of Lidar Depolarization for Characterizing Properties and Phase of Clouds and Precipitation," J. Atmos. Oceanic Technol. **18**(9), 1429–1446 (2001).

55. C. Wang, H. Xia, M. Shangguan, Y. Wu, L. Wang, L. Zhao, J. Qiu, and R. Zhang, "1.5 μm polarization coherent lidar incorporating time-division multiplexing," Opt. Express **25**(17), 20663 (2017).

56. A. Behrendt, T. Nakamura, M. Onishi, R. Baumgart, and T. Tsuda, "Combined Raman lidar for the measurement of atmospheric temperature, water vapor, particle extinction coefficient, and particle backscatter coefficient," Appl. Opt. **41**(36), 7657–7666 (2002).

57. V. Wulfmeyer, R. M. Hardesty, D. D. Turner, A. Behrendt, M. P. Cadeddu, P. Di Girolamo, P. Schlüssel, J. Van Baelen, and F. Zus, "A review of the remote sensing of lower tropospheric thermodynamic profiles and its indispensable role for the understanding and the simulation of water and energy cycles," Rev. Geophys. **53**(3), 819–895 (2015).

58. F. Liu and F. Yi, "Spectrally resolved Raman lidar measurements of gaseous and liquid water in the atmosphere," Appl. Opt. **52**(28), 6884–6895 (2013).

59. D. N. Whiteman, "Examination of the traditional Raman lidar technique. I. Evaluating the temperature-dependent lidar equations," Appl. Opt. **42**(15), 2571–2592 (2003).

60. D. N. Whiteman, "Examination of the traditional Raman lidar technique. II. Evaluating the ratios for water vapor and aerosols," Appl. Opt. **42**(15), 2593–2608 (2003).